Aerospace Science and Technology 107 (2020) 106325

Contents lists available at ScienceDirect

Aerospace Science and Technology

www.elsevier.com/locate/aescte

An experimental study on different plasma actuator layouts for aircraft icing mitigation

Cem Kolbakir [1], Haiyang Hu, Yang Liu, Hui Hu *

Department of Aerospace Engineering, Iowa State University, Ames, IA 50011, United States of America

ARTICLE INFO

Article history:
Received 18 September 2020
Received in revised form 19 October 2020
Accepted 26 October 2020
Available online 29 October 2020
Communicated by Muguru Chandrasekhara

Keywords:
DBD plasma actuation
Plasma-induced thermal effects
Aircraft anti-icing

ABSTRACT

An experimental study was conducted to examine the effects of dielectric-barrier-discharge plasma (DBD) actuator layout on the plasma-induced thermal characteristics and evaluate their effectiveness for aircraft icing mitigation. The experimental investigation was performed in the Icing Research Tunnel of Iowa State University (i.e., ISU-IRT) with an airfoil/wing model embedded with an array of DBD plasma actuators around the airfoil leading edge. The plasma actuators were arranged in different layouts (e.g., orientation, number, and width of exposed electrodes) to evaluate their effects on the anti-icing performance under a typical glaze icing condition pertinent to aircraft inflight icing phenomena. While the dynamics ice accretion or anti-icing process over the airfoil surface before and after turning on the plasma actuators was recorded by using a high-resolution imaging system, a high-speed infrared thermal imaging system was used to quantitatively map the temperature distributions over the airfoil surface. The experimental results clearly reveal that, with the same power consumption level, the plasma actuators in streamwise layout would result in higher plasma-induced surface heating and faster runback of the unfrozen water over the airfoil surface, thereby, having a noticeably better anti-icing performance, in comparison to those in spanwise layout. The plasma actuators in streamwise layout were found to not only be able to prevent ice accretion near the airfoil leading edge, but also allow the plasma-induced surface heating to convect further downstream to delay/prevent the runback ice formation near the airfoil trailing edge. A proper combination of the plasma actuation strength and the plasma discharge coverage over the airfoil surface was found to result in the optimum performance for aircraft anti-icing applications.

1. Introduction

Aircraft icing is a well-known weather hazard to flight safety and performance. With aircraft flying under cold weather conditions, supercooled water droplets in the clouds would impinge, freeze and form ice shapes on airframe surfaces [1]. Ice accretion on the airframe surfaces would cause large-scale flow separations and degrade the aerodynamic performance of aircraft significantly. As a result, aircraft would experience much greater drag and less lift, and stall at a much smaller angle of attack, which could even lead to aircraft crashes [2–4]. While a number of anti-/de-icing methods have been developed for aircraft inflight icing mitigation, current aircraft icing protection strategies suffer from various drawbacks, including being too complex, too heavy or draw too much power to be effective. For example, chemical-based ice removal methods, e.g., use of freezing point depressants to suppress ice formation [5], were found to become less effective at colder temperatures with the ice adhesion strength to airframe surface increases [6]. While mechanical-based de-icing methods, such as using pneumatic or electro-mechanical boots [6,7], have been used to break off ice chunks accreted on wing surfaces, they may pose foreign object damage (FOD) hazards to aero-engines. While thermal-based strategies are widely used to melt ice accreted over airframe surfaces, they usually require substantial power input to keep the airframe surfaces ice free [8–12]. Passive anti-icing methods using hydro-/ice-phobic coatings/materials have also been suggested to reduce ice accretion on airframe surfaces [13–15]. Much efforts are still needed to improve the poor endurance of hydro-/ice-phobic coatings/materials (e.g., mechanical durability and rain erosions due to the high-speed impacting of super-cooled water droplets) under harsh icing conditions [16,17]. It is highly desirable and essential to develop innovative strategies for aircraft icing mitigation and protection for safer and more efficient aircraft operation under atmospheric icing conditions.

Dielectric Barrier Discharge (DBD) plasma actuators are fully electronic devices without any moving parts. They have been used

* Corresponding author.
E-mail address: huhui@iastate.edu (H. Hu).
[1] Present address: Dept. of Aerospace Engineering, the University of Samsun, Turkey.

https://doi.org/10.1016/j.ast.2020.106325
1270-9638/

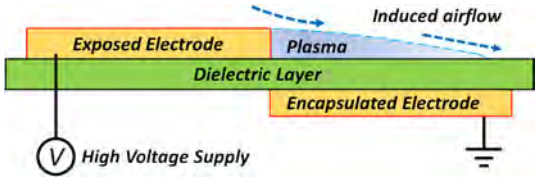

Fig. 1. Schematic of a typical DBD plasma actuator.

extensively in the aerospace engineering community as an effective tool for flow control applications [18–21]. As shown schematically in Fig. 1, a DBD plasma actuator usually features two electrodes attached asymmetrically on the opposite side of a dielectric barrier layer. When a high voltage, either in alternating current (AC) or nanosecond pulses (NS-pulsed), is applied to the electrodes, the air over the encapsulated electrode becomes ionized and generates a streak of plasma. In the presence of a high-intensity electric field, the ionized air would lead to a body force to produce a gas flow along the dielectric surface (i.e., wall jet generation). While the plasma-induced wall jets are widely used to suppress boundary layer flow separation and/or delay airfoil stall, Benard & Moreau [22] found that the electro-mechanical efficiency of a DBD plasma actuator (e.g., the ratio of the energy used to induce ionic wall jet flows to the total energy consumed by the actuator) is usually very low (i.e., no more than 0.20%), and majority of the energy consumed by the plasma actuator would be dissipated via gas heating and dielectric heating. Rodrigues et al. [23] conducted a comprehensive study to investigate the heat generation mechanisms of a DBD plasma actuator. They found that, while dielectric heating is significant near the breakdown voltage, gas heating would become dominate when the applied voltage is above the breakdown voltage. More specifically, as sinusoidal-shaped AC voltages ranging from 2 kV to 10 kV at the same frequency of 24 kHz are applied to a plasma actuator with Kapton as the dielectric material, 70% to 85% of the total power consumption of the DBD plasma actuator would be used for gas heating, whereas roughly 10% of the power consumption would convert into dielectric heating. As a result, while the ambient air over the encapsulated electrodes of plasma actuators would be heated up rapidly during the plasma actuation, the airfoil surface where the plasma actuators were embedded onto would also be heated up subsequently. A number of studies further examined the feasibility of utilizing the thermal effects induced by DBD plasma actuations for aircraft icing mitigation [24–29]. In comparison to conventional electric-heating methods, DBD-plasma-based approach was found to have a more efficient heating mechanism; faster response time; lower operation power consumption; and more stable operation.

The most-commonly-used layout to employ DBD plasma actuators for the flow separation control or/and airfoil stall suppression applications is to embed the electrodes of the plasma actuators near the airfoil leading edges and arrange them along the spanwise direction of the airfoil/wing models. Such a spanwise layout for the DBD plasma actuators was found to be the very effective for flow control applications [30,31]. While the spanwise layout has also been found to be promising in suppressing ice accretion over airfoil surfaces [24,32], a streamwise layout for DBD plasma actuators, i.e., having the exposed electrodes of DBD plasma actuators oriented along the chordwise direction of airfoil/wing models, was also suggested and demonstrated to have a very good performance for aircraft anti-icing applications [29,33,34]. In spite of the noticeable advances made in recent years to demonstrate the feasibility of leveraging plasma-induced thermal effects for aircraft anti-icing applications, much more studies are still needed to explore/optimize design paradigms for the development of a new class of plasma-based icing protection strategies to ensure safer and more efficient operation of aircraft in cold weathers.

In the present study, a comprehensive experimental campaign was conducted to evaluate the effects of different layouts of DBD plasma actuators embedded over the surface of an airfoil/wing model on the plasma-induced thermal characteristics and examines their performance for aircraft icing mitigation. The experimental study was performed in the Icing Research Tunnel of Iowa State University (i.e., ISU-IRT). An array of DBD plasma actuators was flush mounted around the leading edge of a NACA0012 airfoil/wing model in different layouts (i.e., spanwise vs. streamwise layout with varied numbers and width of the exposed electrodes). During the experiments, while the airfoil/wing model was exposed to a typical glaze icing condition, the power inputs supplied to the DBD plasma actuators in different layouts were kept at the same value for the anti-icing operation. In addition to utilizing a high-resolution imaging system to record the dynamic ice accretion or anti-icing process over the surface of the test model, a high-speed Infrared (IR) thermal imaging system was also used to quantitatively map the temperature distributions over the airfoil surface before and after turning on the DBD plasma actuators. The acquired ice accretion images were correlated with the quantitative IR thermal imaging results to elucidate the underlying physics to better understand the effects of the plasma actuator layout on the plasma-induced thermal characteristics and their performances to suppress ice accretion over airfoil surface.

2. Experimental setup and the test model

2.1. Icing research tunnel used in the present study

The experimental study was performed in ISU-IRT. As shown schematically in Fig. 2, ISU-IRT is a research-grade, multi-functional icing research tunnel with a test section of 2.0 m in length $\times$ 0.4 m in width $\times$ 0.4 m in height and four transparent side walls. It can generate wind speed up to 60 m/s and airflow temperature down to $-25\,^{\circ}C$ in the test section. An array of eight pneumatic atomizer/spray nozzles is installed at the entrance of the contraction section of ISU-IRT to inject micro-sized water droplets (10 $\sim$ 100 μm in size) into the airflow. A variable *LWC* levels in ISU-IRT (i.e., ranging from 0.1 g/m^3 to 5.0 g/m^3) can be achieved by manipulating the pressure and flow rate supplied to the atomizer/spray nozzles. In summary, ISU-IRT can be used to simulate various atmospheric icing phenomena over a range of icing conditions (i.e., from dry *rime* to extremely wet *glaze* ice conditions). Further information about ISU-IRT and its usage for various icing and anti-icing studies is available in Waldman et al. [35], Liu et at. [26], Gao et al. [36], Li et al. [37] and Veerakumar et al. [38].

2.2. The airfoil/wing model used in the present study

In the present study, a two-dimensional airfoil/wing model with NACA0012 airfoil profile in the cross section was used for the experimental investigation. The airfoil/wing model has a chord length of $C = 150$ mm and spanwise length of 400 mm (i.e., with the same dimension as the width of the ISU-IRT test section). The test model was 3D printed by using a rapid prototyping machine (i.e., Stratatsys® CONNEX1 OBJET260) in two half-spanned pieces with a hollowed cross section and made of a hard plastic material (i.e., Stratatsys® Vero White). The two 3D printed model pieces were assembled almost seamlessly and glued together by adding a small amount of super glue (Starbond® CA Glue) along the interface. The surface of the test model was wet sanded by using a series of progressively finer sandpapers (up to 2,000 grit). The final surface of the test model was found to have a very smooth, glossy finish with a characteristic surface roughness about 20 μm. Supported by stainless-steel rods, the airfoil/wing model was mounted

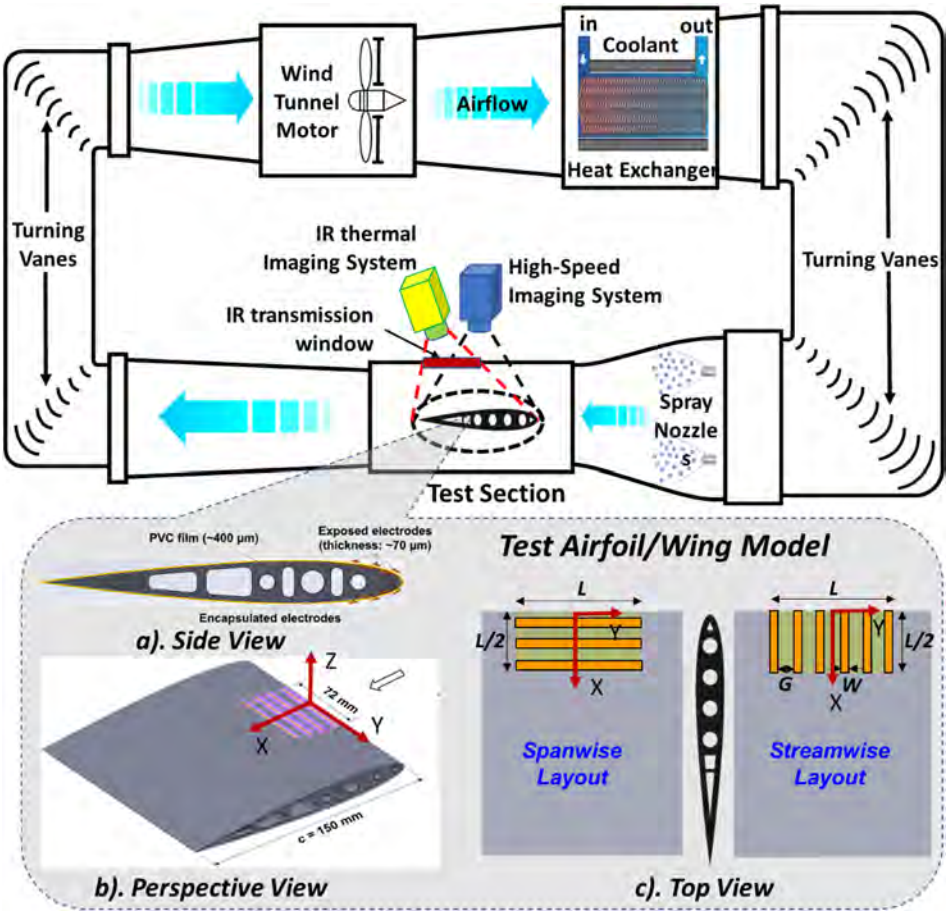

Fig. 2. Schematic of ISU-IRT and the airfoil/wing model used in the present study.

Table 1
A list of the test cases investigated in the present study.

Test Case #	Plasma Actuator Layout	Number of exposed electrodes, (N)	Gap between exposed electrodes, (G)	Width of exposed electrodes, (W)	Edge length of exposed electrodes, (L_{edge})	Applied voltage for plasma actuation, ($V_{p\text{-}p}$)
1	Spanwise	6	8.0 mm	4.0 mm	910 mm	13.8 kV
2	Streamwise	6	8.0 mm	4.0 mm	910 mm	13.8 kV
3	Streamwise	8	8.0 mm	2.0 mm	1180 mm	12.2 kV
4	Streamwise	5	8.0 mm	8.0 mm	800 mm	15.4 kV
5	Streamwise	3	8.0 mm	16.0 mm	530 mm	16.0 kV

horizontally in the middle of the ISU-IRT test section with the angle of attack (AOA) of the test models being zero in relation to the incoming airflow (i.e., AOA = 0°). During the experiments, the velocity and temperature of the incoming airflow was kept at $V_\infty = 40$ m/s and $T_\infty = -5\,°C$ for the present study. The corresponding chord Reynolds number is $Re_c \approx 500{,}000$.

As shown in Fig. 2, DBD plasma actuators were wrapped around the leading edge of the airfoil/wing model. The plasma actuators were made "in-house" using ~70 μm thick copper tapes to function as electrodes and Polyvinyl chloride (PVC) film of ~400 μm in thickness as the dielectric layer. While the exposed electrodes have the same length of $L = 72$ mm, the width of the electrodes is varied from $W = 4.00$ mm to 16.0 mm for different test cases as summarized in Table 1. During the experiment, sinusoidal AC voltages ranging from 12 kV to 16 kV were applied to the plasma actuators at the same frequency of 5.5 kHz. The exposed electrodes were subjected to high voltage, while the encapsulated electrode was connected to the ground.

In order to evaluate the effects of the DBD plasma actuator layout on the plasma-induced thermal characteristics and the resultant effectiveness for aircraft icing mitigations, the plasma actuators were arranged in either spanwise or streamwise layout (i.e., with the exposed electrodes being arranged either spanwise or chordwise over the airfoil surface). Table 1 summarizes all the test cases to be explored. While the encapsulated electrode of the DBD plasma actuator were kept to have the same coverage area of 72 mm × 72 mm for all the test cases, the orientation, total number (N), and the width (W) of the exposed electrodes were varied for a comparative study. As a result, the coverage area of the plasma discharges (i.e., the area with plasma glow) would be varied by changing the number and width of the exposed electrodes.

During the experiments, DBD plasma actuators embedded over the airfoil/wing surface were powered by a high-voltage AC power source (Nanjing Suman, model CTP-2000K). The electric voltage and current applied to the plasma actuators were measured by using a Textronix P6015 high-voltage Probe and Pearson Current

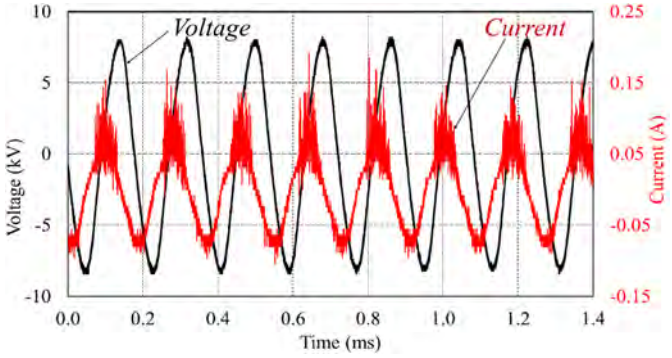

Fig. 3. Typical voltage and current trace during the plasma actuation.

Monitor. While the voltage and current signals were monitored by using a Tektronix MDO3102 mixed domain oscilloscope, the power consumption of the plasma actuators was calculated by using following equation:

$$P = \frac{1}{T}\int_0^T V(t) \times I(t)dt \tag{1}$$

where $V(t)$ and $I(t)$ are the instantaneous voltage and current applied on the plasma actuators, and T is the total measurement time (i.e., about 5.0 minutes for each test cases in the present study). Fig. 3 gives an example of the typical voltage and current traces (i.e., containing about eight AC periods). Using an autotransformer, the total power inputs supplied to the plasma actuators were fixed at $P = 64 \pm 2.5$ W during the experiments. The corresponding power density applied to the plasma actuators for the anti-icing operation was estimated to be $P_d = P/A_P = 12.2 \pm 0.5$ kW/m^2, where A_P is the coverage area of the encapsulated electrode (i.e., 72 mm × 72 mm) over the airfoil/wing model.

2.3. Measurement technique used in the present study

As shown schematically in Fig. 2, a high-resolution digital imaging system (i.e., PCO Tech, PCO1200^{TM} camera with a spatial resolution of 1248 pixels × 1280 pixels) along with a 60 mm optical lens (Nikon, 60 mm Nikkor 2.8D) was used to record the dynamic ice accretion or anti-icing process over the airfoil surface before and after turning on the plasma actuators. The corresponding temperature distributions over the airfoil surface were mapped with an IR thermal imaging system with a spectral range of 7.5 ∼ 14 μm (i.e., FLIR-A615 with 640 pixels × 480 pixels in spatial resolution) during the anti-icing process. It should be noted that, an IR transmission window (i.e., FLIR IRW-4C) was embedded on the top panel of the ISU-IRT test section for the IR thermal image acquisition. Before turning on the plasma actuators for the anti-icing experiments, the IR thermal imaging system was calibrated against the measured surface temperatures using an array of thermocouples embedded on the surface of the test model. Further information about the calibration procedure of the IR thermal imaging system can be found in Liu et al. [39]. More examples of using IR thermal imaging systems to characterize plasma-induced thermal effects and to study dynamic ice accretion processes can be found in Liu et al. [25], Joussot et al. [40], Cai et al. [28], Li et al. [41] and Gao et al. [42]. The uncertainty for the surface temperature measurement results reported in the present study was found to be within ±0.2 °C.

3. Measurement results and discussions

Before performing the icing or anti-icing experiments, ISU-IRT was operated at a prescribed incoming airflow velocity and temperature (i.e., V_∞ = 40 m/s and $T_\infty = -5$ °C for the present study) for at least 30 min in order to ensure that ISU-IRT reached a thermal steady state. Then, the DBD plasma actuators embedded over the surface of the airfoil/wing model were turned on for the anti-icing operation. The high-speed digital imaging system and IR thermal imaging system were synchronized with the plasma actuators to characterize the dynamic plasma actuation and unsteady heat transfer process over the airfoil surface simultaneously.

As described above, by leveraging the thermal effects induced by DBD plasma actuation, plasma actuators in either spanwise or streamwise layout have been demonstrated to be able to prevent ice formation/accretion over airfoil surfaces. However, no systematic studies have ever been conducted to provide a side-by-side comparison to reveal which layout (i.e., spanwise vs. streamwise) would be more favorable for aircraft icing protection. A comparative investigation was conducted in the present study to characterize the effects of the orientation of the plasma actuators on the plasma-induced thermal characteristics and the resultant anti-icing performances. As shown schematically in Fig. 2, the same six sets of DBD plasma actuators were embedded over the surface of the same airfoil/wing model in either spanwise or streamwise layout (i.e., the test case #1 and #2 listed in the Table 1). It should be noted that, the exposed electrodes were arranged symmetrically over the upper and lower surfaces of the airfoil/wing model, therefore, only three exposed electrodes were shown on the upper surface of the airfoil/wing model for the test case #1 with the plasma actuators in the spanwise layout.

3.1. Effects of orientation of the plasma actuators on plasma-induced thermal characteristics

Fig. 4 shows typical measurement results of the IR thermal imaging system to show the distributions of the temperature increase (i.e., $\Delta T = T_{surface}$-$T_{ambient}$) on the airfoil surface after 60 seconds of the DBD plasma actuation. The measurement results were obtained under the "dry" test condition, i.e., without turning on the water spray system of ISU-IRT. While the test model was exposed in the frozen cold airflow of $T_\infty = -5$ °C, the measurement results indicate that the surface temperatures of the airfoil/wing model became substantially higher (i.e., ΔT increasing up to 40 °C) than the ambient airflow temperature, due to thermal effects induced by the DBD plasma actuation. The regions with the highest temperature values were consistently found to be along the edges of the exposed electrodes where the DBD plasma discharges are generated. As shown clearly in Fig. 4(a), for the test case with the exposed electrodes of the plasma actuators in spanwise layout (i.e., the test case #1), the surface temperature distribution was found to be rather uniform along the edges of the spanwise aligned exposed electrodes (i.e., the region with plasma glow). However, for the test case with the plasma actuators in streamwise layout (i.e., the test case #2), the measured surface temperatures were found to increase monotonically along the edges of the exposed electrodes, as shown clearly in Fig. 4(b). Despite the power inputs supplied to the plasma actuators were set to be the same for the two compared test cases, the size of the heated regions with relatively high temperatures over the airfoil surface was found to be larger for the test case with the plasma actuators in streamwise layout, in comparison to those of the case with the electrodes in spanwise layout. Obvious "heat streaks" can also be seen in the downstream of the electrodes for the case with the plasma actuators in streamwise layout.

Based on the IR thermal imaging results as those given in Fig. 4, the surface temperature profiles over the airfoil surface at four typical downstream locations (i.e., at $X/C = 7\%$, 15%, 25% and 35% as indicated by the dashed lines in Fig. 4) were extracted, and the results are plotted in Fig. 5. The effects of the plasma actuator

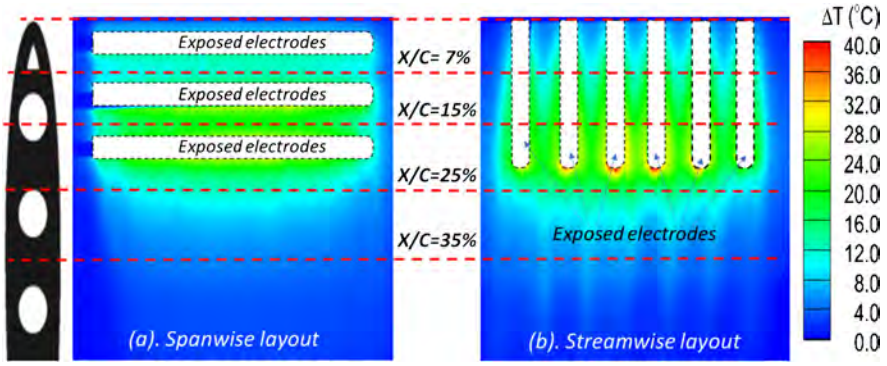

Fig. 4. Measured surface temperature distributions after turning on the DBD plasma actuators for 60 seconds under the dry test conditions of $V_\infty = 40$ m/s and $T_\infty = -5\,^\circ$C. (For interpretation of the colors in the figure(s), the reader is referred to the web version of this article.)

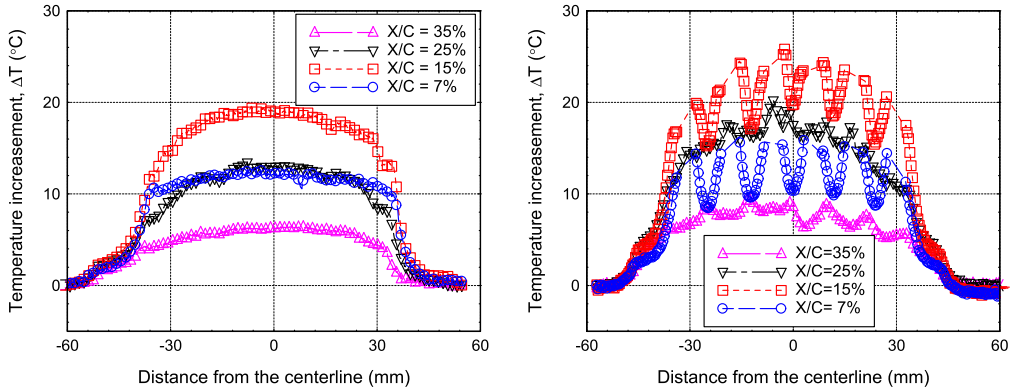

(a). Plasma actuators in spanwise layout (b). Plasma actuators in streamwise layout

Fig. 5. Temperature profiles extracted at different downstream locations over the airfoil surface with the DBD plasma actuators in either spanwise or streamwise layout.

layout (i.e., spanwise vs. streamwise) were revealed more quantitatively based on the side-by-side comparison of the measured surface temperature profiles. Since the plasma induced gas heating occurs mainly along the edges of the exposed electrodes [23], the resultant temperature increases (i.e., ΔT values) over the airfoil surface were found to be rather uniform along the spanwise direction of the airfoil/wing model for the test case with the plasma actuators in spanwise layout (i.e., for the test case #1). In comparison, the surface temperature increases (i.e., ΔT values) were found to fluctuate greatly along the spanwise direction for the test case with the plasma actuators in streamwise layout, as shown in Fig. 4(b). Corresponding to the generation of plasma glows at the edges of the exposed electrodes, the measured surface temperatures were found to be much higher (i.e., reaching the local peak values) at the edges of the exposed electrodes, and the surface temperatures were found to become much lower in the gaps between the neighboring electrodes. It can also been seen that, despite the key operation parameters for the DBD plasma actuation (i.e., the applied electric voltage and power input, the dielectric layer type and thickness, the size of the encapsulated electrode, the width and numbers of the exposed electrodes, etc.) were set to be the same for the two compared test cases, the surface temperatures on the airfoil/wing model for the test case with the plasma actuators in streamwise layout (i.e., the test case #2) were found to be up to $\sim 5.0\,^\circ$C higher than those of the spanwise layout case (i.e., the test case #1) at the selected downstream locations given in Fig. 5.

In order to quantitatively characterize the global effects of the plasma actuator layout on the plasma-induced thermal characteristics over the airfoil surface, the variations of the spatially-averaged surface temperatures in two selected windows over the airfoil surface were examined as a function of the time after turning on the plasma actuators. As shown schematically in Fig. 6, while the interrogated window #1 is selected to represent the region protected by the plasma actuators (i.e., from the airfoil leading edge (LE) to 25% chord downstream), the interrogated window #2 is located at the downstream of the region protected by the plasma actuators (i.e., from 25% chord to 50% chord). It can be seen clearly that, after the DBD plasma actuators were turned on at the time instant of $t = 0$ s, the spatially-averaged temperatures over the airfoil surface were found to increase rapidly for both the streamwise and spanwise layout cases. Despite the incoming airflow conditions and the power inputs supplied to the plasma actuators were kept at the same during the experiments, the averaged surface temperatures over the region protected by the plasma actuators (i.e., the interrogated window #1) were found to be about $\sim 3.0\,^\circ$C higher for the test case with the plasma actuators arranged in streamwise layout (i.e., the test case #2), in comparison to those of the spanwise layout case (i.e., the test case #1). Likewise, the averaged temperatures over the airfoil surface in the downstream region for the streamwise layout case were still found to be about $\sim 1.0\,^\circ$C higher than those of the spanwise layout case. Since higher surface temperatures over the airfoil surface are more desirable for anti-icing applications, the quantitative measurement results indicate that, with the same power input supplied to the plasma actuators, the design with the plasma actuators arranged in streamwise layout would be more favorable than those in spanwise layout for aircraft icing mitigation.

Fig. 7 illustrates how the plasma actuators in different layout will interact with the airflow over the airfoil surface. This further explains why the DBD plasma actuators arranged in streamwise layout would induce higher temperatures over the airfoil surface, in comparison to the spanwise layout case. It is well known that, after turning on the DBD plasma actuator, while wall jets would

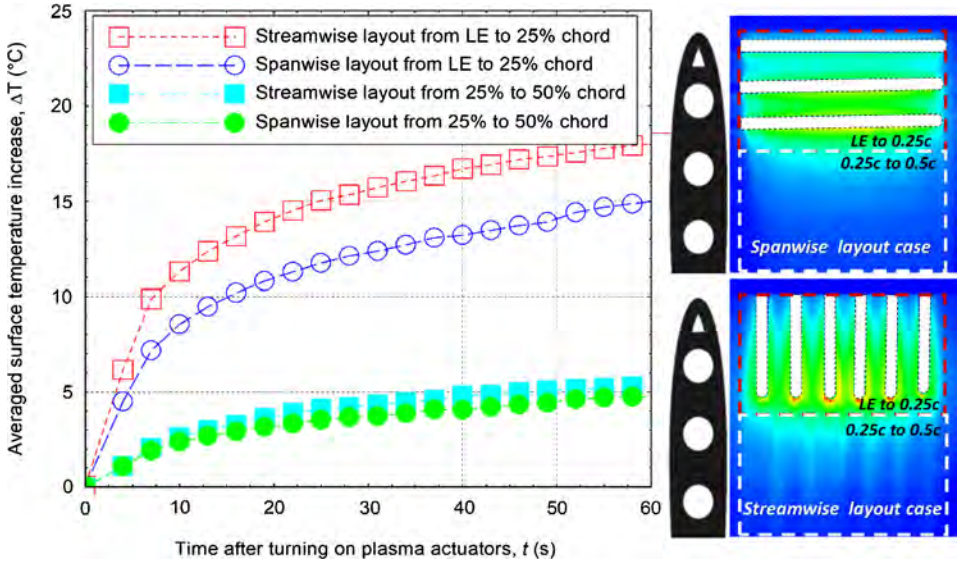

Fig. 6. Averaged surface temperature in time over the surface of the test model with the DBD plasma actuators arranged in either spanwise or streamwise layout under the dry test conditions of $V_\infty = 40$ m/s and $T_\infty = -5\,^\circ$C.

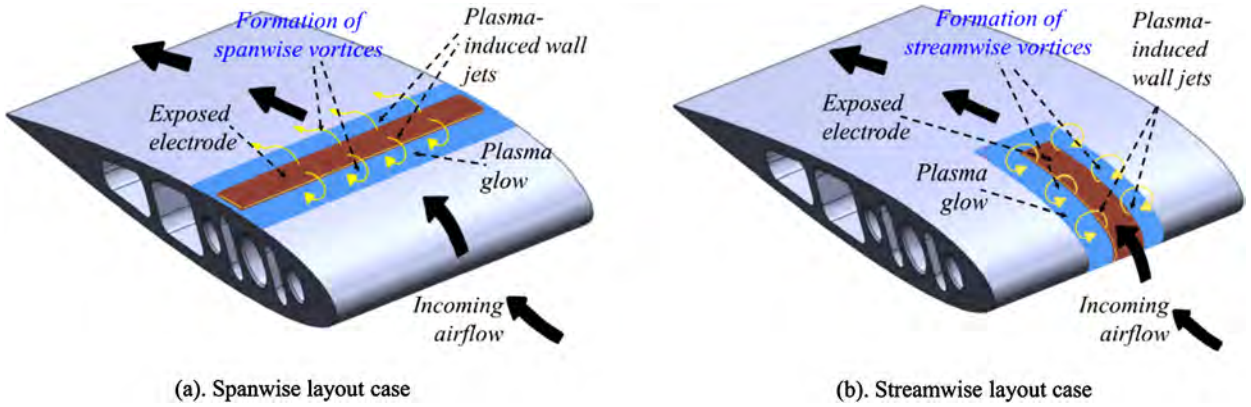

Fig. 7. Schematics to illustrate the effects of plasma actuator layout on the interactions of the plasma-induced wall jets and the incoming airflow over an airfoil surface.

be generated along the edges of exposed electrodes [20,43], the plasma-induced thermal effects would also heat up the airfoil surface as revealed quantitatively from the IR thermal imaging results given in Figs. 4 to 6. For the case with the plasma actuator in spanwise layout, the direction of the incoming airflow is normal to the orientation of the exposed electrode of the plasma actuator. The exposed electrode acts as a turbulator to perturb the boundary layer airflow over the airfoil surface. As shown schematically in Fig. 7(a), the plasma-induced wall jets would also interact with the incoming airflow intensively to induce spanwise vortices along the long edges of the exposed electrode, which is especially true for the plasma-induced wall jets generated along the leading edge of the exposed electrode with the direction of the wall jet being opposite to the incoming airflow. The turbulator effects of the exposed electrode and the interactions between the plasma-induced wall jets and the incoming airflow promote a faster transition of the boundary layer airflow from laminar to turbulence over the airfoil surface. The faster boundary layer flow transition augments the convective heat transfer between the heated airfoil surface and the frozen-cold incoming airflow. As a result, the plasma-induced thermal effects would be dissipated much faster via convective heat transfer to the frozen-cold airflow over the airfoil surface for the spanwise layout case. The faster dissipation of the plasma-induced thermal effects would result in lower surface temperatures on the airfoil surface, as revealed quantitatively from the IR thermal imaging results given above.

For the test case with the plasma actuators in streamwise layout, as shown schematically in Fig. 7(b), since the orientation of the exposed electrode is aligned with the direction of the incoming airflow, the air stream would be able to flow over the airfoil surface more smoothly with much less disturbances, in comparison to the spanwise layout case discussed above. As described in Jukes & Choi [44], the streamwise oriented DBD plasma actuators would also act as vortex generators to re-energize near wall airflow by producing a spanwise body force and result in the formation of counter-rotating streamwise vortex structures at two sides of the exposed electrodes. The streamwise vortex structures would induce a wider spreading of the plasma-induced gas heating along the lateral direction to cover larger airfoil surface. Consequently, the coverage of the regions with relatively high temperatures over the airfoil surface were found to become greater with the plasma actuators in streamwise layout than those of the spanwise layout case, which was confirmed quantitatively by the IR thermal imaging results given in Fig. 4. It should also be noted that, the downwash induced by the streamwise vortex structures at the two sides of each exposed electrodes would also enable a longer stay of the heated air (i.e., the airflow heated by the plasma-induced gas heating effects along the edges of the exposed electrodes) near the airfoil surface while moving to further downstream region. This re-

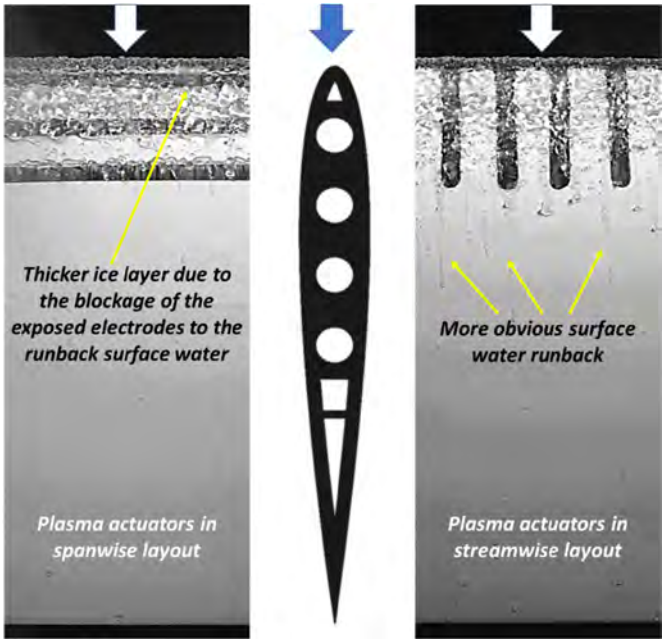

Fig. 8. Acquired images of the accreted glaze ice structures after 150 seconds of the icing experiment with $V_\infty = 40$ m/s, $T_\infty = -5.0\,^\circ$C and LWC=1.5 g/m^3 and plasma actuators turning off.

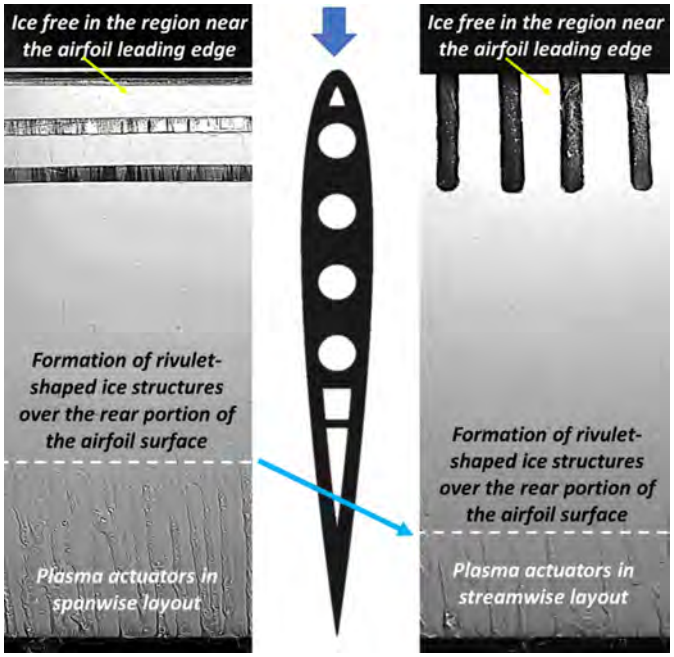

Fig. 9. The acquired snapshot images of anti-icing operation on the airfoil surface under the test condition of $V_\infty = 40$ m/s, $T_\infty = -5.0\,^\circ$C and LWC=1.5 g/m^3 and plasma actuators turning on.

sults in the existence of the "hot" streaks extending far beyond the area protected by the plasma actuators, which are also revealed clearly from the IR thermal imaging results given in Fig. 4.

3.2. Effects of the orientation of the plasma actuators on the anti-icing performance

In the present study, a comparative study was also conducted to examine the effects of the layout (i.e., spanwise vs. streamwise) of DBD plasma actuators embedded over the airfoil surface on their effectiveness for aircraft icing mitigations. For the anti-icing experiments, while the ISU-IRT was operated to generate a typical glaze icing condition with $V_\infty = 40$ m/s, $T_\infty = -5.0\,^\circ$C and LWC=1.5 g/m^3, the same sinusoidal-shaped AC voltage of 13.8 kV was applied to the plasma actuators at the same frequency of 5.5 kHz.

Similar as the scenario described in Liu et al. [39], after switching on the water spray system of ISU-IRT, the micro-sized water droplets exhausted from the spray nozzles would become super-cooled droplets. If no anti-icing measures are employed (i.e., without turning on the plasma actuators), dynamic ice accretion was found to start immediately as the super-cooled water droplets impacted onto the airfoil surface. Fig. 8 gives the typical snapshot images of the ice structures accreted over the surface of the airfoil/wing model after 150 seconds of the ice accretion process for the test case without turning on the DBD plasma actuators. The ice accretion process over the airfoil surface was found to be of a typical glaze ice accretion process, which manifests as transparent, glassy ice structures near the airfoil leading edge with obvious water runback at further downstream, similar as that described in Waldman & Hu [35].

Based on the side-by-side comparison of the acquired ice accretion images given in Fig. 8, some noticeable differences can be identified for the accreted ice structures over the surface of the airfoil/wing model with the embedded plasma actuators in spanwise layout, in comparison to those of the spanwise layout case. Despite of their small thickness (i.e., $\sim$ 70 μm), the exposed electrodes of the plasma actuators would act as turbulators to the boundary layer airflow and interact with the runback water flow over the airfoil surface. As shown clearly in Fig. 8, the spanwise-oriented exposed electrodes (i.e., the plasma actuators in spanwise layout) act as obstacles to slow down the runback of the surface water flow, thereby, delaying the transport of the impacted water from the airfoil front surface to further downstream locations. This caused the accumulation of more impacted water in the region near the airfoil leading edge. As a result, ice layer accreted along the leading edge of the airfoil/wing model was found to be much thicker for the test case with the plasma actuators in spanwise layout (i.e., at the left side of Fig. 8), in comparison to the streamwise layout (i.e., at right side of Fig. 8). Additionally, for the plasma actuators in streamwise layout, the exposed electrodes were oriented along the direction of the incoming airflow, allowing a smoother runback of the surface water over the airfoil surface. This enables a fast transport of the impinged water from the front airfoil surface to further downstream locations before the runback water was frozen into ice. As revealed clearly in the snapshot images of the ice accretion given in Fig. 8, more obvious surface runback can be seen in the form of multiple rivulet flows over the airfoil surface for the test case with the plasma actuators in streamwise layout.

Fig. 9 shows the acquired images to reveal the anti-icing process over the airfoil surface with the DBD plasma actuators being turned on. During the experiments, same power input of $P = 64$ W (i.e., the applied peak-to-peak voltage of $V_{P\text{-}P} = 13.8$ kV and AC frequency of $f = 5.5$ kHz) was supplied to the DBD plasma actuators. The DBD plasma actuators either in spanwise or streamwise layout were turned on for 60 seconds before switching on ISU-IRT water spray system. The snapshot images given in Fig. 9 were acquired after turning on the water spray system of ISU-IRT for 150 seconds. As shown clearly in Fig. 4 and Fig. 5, regardless of the plasma actuator layout, the temperatures over the front surface of the airfoil/wing model (i.e., the region protected by the plasma actuators) were found to be well above the frozen temperature of water, due to the plasma-induced thermal effects. Upon impinging onto the heated front surface of the test model (i.e., mainly within the direct impingement zone of the super-cooled water droplets near the airfoil leading edge [39]), the super-cooled water droplets would be heated up rapidly. As a result, instead of accreting ice, a layer of "warm" water film was found to accumulate over the front

surface of the airfoil/wing model. In summary, no ice was found to form/accrete over the front surface of the airfoil/wing model after the plasma actuators were turned on, as revealed clearly from the snapshot images given in Fig. 8.

Similar as those described in Zhang et al. [45], the unfrozen water mass collected in the front region near the airfoil leading edge (i.e., mainly within the direct impingement zone of the supercooled water droplets as described in Liu and Hu [39]) was found run back rapidly, as driven by the boundary layer airflow over the airfoil surface. As shown clearly in Fig. 9, with the surface water film advancing to further downstream, multiple rivulet flows were found to form on the rear portion of the airfoil surface. This resulted in the formation of multiple isolated water transport channels to convey the impacted water mass collected in the region near the airfoil leading edge (i.e., due to the continuous impingement of the super-cooled water droplets onto the airfoil surface) to further downstream regions (i.e., beyond the direct impinging zone of the supercooled water droplets near the airfoil leading edge).

It should also be noted that, since the incoming airflow surrounding the airfoil/wing model was kept at the frozen-cold temperature of $T_\infty = -5.0\,^\circ$C during the experiment, the runback surface water would be cooled down continuously as flowing into the "unheated" downstream region, i.e., the unprotected airfoil surface on the rear portion of the airfoil/wing model. As a result, while the fast runback of the surface water would make a portion of the runback surface water to shed off from the airfoil trailing edge, the rest of the surface water was found to be frozen into ice subsequently before reaching to the airfoil trailing edge. Therefore, rivulet-shaped ice structures were found to accrete over the rear surface near the trailing edge of the airfoil/wing model, as revealed clearly from the acquired snapshot images given in Fig. 9.

It can also be seen that, even though the same airfoil/wing model was exposed under the same glaze icing conditions and the same power inputs were supplied to the plasma actuators for the anti-icing operation, the locations where to start forming the rivulet-shaped ice structures were found to be quite different for the two compared cases. While rivulet-shaped ice structures were found to start to form on the rear surface of the airfoil/wing model since the downstream location of $X/C \approx 65\%$ for the test case with the plasma actuators in the spanwise layout, the formation of the rivulet-shaped ice structures was found to be delayed substantially (i.e., up to the downstream location of $X/C \approx 78\%$) for the streamwise layout case. Besides the much later formation of the rivulet-shaped ice structures over the airfoil surface, the total amount of the ice structures accreted over the airfoil surface was also found to become much less for the streamwise layout case. The delayed formation of the rivulet-shaped ice structures and the much less ice accretion over the airfoil surface for the streamwise layout case is found to coordinate well with the higher surface temperatures and larger coverage of the heated area on the airfoil surface revealed quantitatively from the IR imaging results given in Fig. 4. As described above and shown schematically in Fig. 7, for the test case with the plasma actuators in spanwise layout, the spanwise-oriented exposed electrodes and the plasma-induced wall jets generated along the front edges of the exposed electrodes would slow down the runback of the surface water to cause a longer duration of the runback water staying on the airfoil surface, increasing the possibility of the runback water to be frozen into rivulet-shaped ice structures over the rear portion of the airfoil surface. In comparison, the streamwise oriented plasma actuators would enable a much smoother and faster runback of the surface water from the airfoil leading edge to the trailing edge, therefore, causing less ice formation on the airfoil surface as revealed clearly in the acquired image given in Fig. 9.

It should be noted that, for the test cases given in Fig. 9, since the power input level supplied to the plasma actuators for the anti-/de-icing is relatively low (i.e., $P_d = 12.2$ kW/m^2), while the front surface of the airfoil/wing model was found to be ice free due to the thermal effects induced by the plasma actuation, rivulet-shaped ice structures were found to form on the rear surface of the airfoil/wing model. After increasing the power inputs to the plasma actuators slightly, the formation of the rivulet-shaped ice structures on the rear surface of the airfoil/wing model was found to be suppressed completely. As a result, the entire airfoil surface was found to become totally ice free during the entire duration of the icing experiment. While the minimum power density level to keep the entire airfoil surface ice free for the spanwise layout case was found to be $P_d \approx 15.0$ kW/m^2 [26], the corresponding value was found to be $P_d \approx 13.5$ kW/m^2 for the test case with the plasma actuators in streamwise layout (i.e., ~10% energy saving). In summary, the findings of the present study reveal clearly that, with the fixed power inputs for DBD plasma actuation, the plasma actuators arranged in streamwise layout would be more effective than those in spanwise layout for aircraft anti-icing operation.

3.3. Effects of the width and number of exposed electrodes on the anti-icing performance

An experimental investigation was also conducted to further examine the effects of other design parameters of DBD plasma actuators (e.g., the total numbers and the width of the exposed electrodes) on their performance for aircraft icing mitigation. Since the experimental results given above revealed clearly that the DBD plasma actuators in streamwise layout would be more favorable than the spanwise layout case for anti-icing applications, only the design with the DBD plasma actuators in streamwise layout were considered in this section.

As aforementioned, all the test cases were designed to have the same encapsulated electrode (i.e., with the fixed dimension of 72.0 mm × 72.0 mm embedded over the front surface of the airfoil/wing model). While the gap (G) between the neighboring exposed electrodes were set to be the same (i.e., $G = 8.0$ mm), the total numbers (N) of the exposed electrodes were changed for $N = 3$ to $N = 8$, the corresponding width (W) of the exposed electrodes varied from $W = 16.0$ mm to $W = 2.0$ mm, respectively. By changing the total numbers (N) and width (W) of the exposed electrodes, the total edge length of the exposed electrodes would vary substantially. It should be noted that, since DBD plasma discharges would be generated mainly along the edges of the exposed electrodes [24,34,46,47], the coverage of the DBD plasma glow over the surface of the airfoil/wing model would vary greatly for different test cases. As a result, the electric voltage supplied to the exposed electrodes for DBD plasma actuation would need to be adjusted in order to make sure that the total power inputs supplied to the DBD plasma actuators to stay at the same level for all the compared test cases. Table 1 summarized the total edge length of the exposed electrodes and the applied voltages for DBD plasma actuation for all the test cases. It can be seen that, while the electric voltage supplied to the exposed electrodes was set to be $V_{p\text{-}p} = 16.0$ kV for the test case with the widest exposed electrodes (i.e., $W = 16.0$ mm, which is also the case with the least number of the exposed electrodes of $N = 3$), the corresponding value was found to be $V_{p\text{-}p} = 12.2$ kV for the case with the narrowest exposed electrodes of $W = 2.0$ mm (i.e., the case with the maximum number of the exposed electrodes of $N = 8$).

Fig. 10 shows typical snapshot images acquired during the anti-icing experiments for all the four compared test cases with the plasma actuators arranged in streamwise layout. While the experiments were conducted under the same glaze icing conditions of $V_\infty = 40$ m/s, $T_\infty = -5.0\,^\circ$C and $LWC = 1.5$ g/m^3, and the same power input level of $P_d = 12.2$ kW/m^2 were supplied to the plasma actuators for the anti-icing application, the snapshot im-

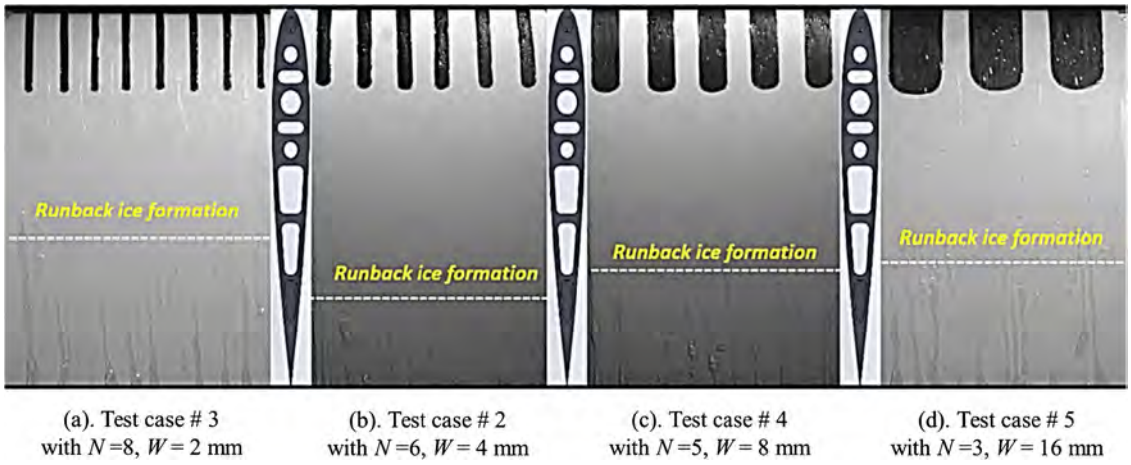

Fig. 10. The acquired snapshot images for the four compared cases after 150 seconds of the anti-icing experiments with $V_\infty = 40$ m/s, $T_\infty = -5.0\,^\circ$C and LWC=1.5 g/m^3.

ages were captured after turning on the DBD plasma actuators for 150 seconds. The corresponding IR thermal imaging results along with the measured surface temperature profiles extracted from the IR thermal imaging maps were given in Fig. 11 for a quantitative comparison of the four test cases.

It can be seen clearly that, with the plasma actuators being turned on, the front surface of the airfoil/wing model (i.e., the area embedded with the plasma actuators) would stay "hot" with the surface temperatures of the airfoil/wing model being well above the water frozen temperature for all the four test cases (i.e., up to $\sim 30\,^\circ$C along the edges of the exposed electrodes). Instead of accreting ice, a layer of water film was found to from over the front surface near the airfoil leading edge. As shown clearly in the snapshot images given Fig. 10, the front surface of the airfoil/wing model was found to be ice free for all the four compared test cases. Driven by the incoming airflow, the unfrozen surface water collected in the front region near the airfoil leading edge (i.e., mainly within the direct impingement zone of the water droplets) was found to run back swiftly along the airfoil surface and forms multiple water rivulets at further downstream locations. As the runback surface water flowing out of the "hot" region (i.e., the region protected by the plasma actuators), a portion of the runback water was found to be cooled down gradually, and was frozen into ice subsequently, resulting in the formation of rivulet-shaped ice structures over the rear surface of the airfoil/wing model, as shown clearly in Fig. 10.

Even though the total power input supplied to the plasma actuators were kept at the same level of $P_d = 12.2$ kW/m^2 during the experiments, the starting points to form rivulet-shaped ice structures on the rear surface of the airfoil/wing model were found to vary noticeably for the compared four test cases. As indicated by the dashed lines given in Fig. 10, the test case having the longest edge length of the exposed electrodes (i.e., the test case #3) was found to have the earliest formation of the rivulet-shaped ice structures at the downstream location of $X/C \approx 60\%$. In comparison, the formation of the rivulet-shaped ice structures was found to start at the downstream location of X/C $\approx$ 66% for the test case with the shortest edge length of the exposed electrodes (i.e., the test case #5). The corresponding downstream locations for the other two test cases, i.e., the test case #2 with $N = 6$, $W = 4.0$ mm and the test case #3 with $N = 5$, $W = 8.0$ mm, were found to be at $X/C \approx 78\%$ and $X/C \approx 68\%$, respectively.

The experimental results described above were found to be correlated well with the characteristics of the measured temperature distributions on the airfoil surface revealed quantitatively from the IR thermal imaging results given in Fig. 11. As reported by Rodrigues et al. [48], DBD plasma discharges would be generated mainly along the edges of the exposed electrodes. For the test case #3 with $N = 8$, $W = 2.0$ mm, since this configuration has the longest edge length for the exposed electrodes, it would have the largest coverage of the plasma glow among the four compared test cases. However, since the total power input supplied to the plasma actuators was kept at the same level during the experiments, the electric voltage applied to the exposed electrodes for the test case #3 was the lowest (i.e., $V_{p\text{-}p} = 12.2$ kV), as listed in Table 1. As a result, the strength of the plasma discharges generated along the edges of the exposed electrodes for this test case would be the weakest, which induce the weakest thermal effects for the anti-icing operation. As revealed quantitatively from the IR thermal imaging results given in Fig. 11(a), the resultant surface temperature increases (i.e., ΔT values) induced by the DBD plasma actuation were found to be the lowest among the four compared test cases. Therefore, such a layout was found to have the earliest formation of the rivulet-shaped ice structures among the four compared cases (i.e., starting from the downstream location of $X/C \approx 60\%$), as shown in Fig. 10.

On the other hand, the strength of the DBD plasma discharges generated along the edges of the exposed electrodes for the test case #5 would be the strongest among the four compared test cases, due to the highest applied electric voltage to the exposed electrodes (i.e., $V_{p\text{-}p} = 16.0$ kV). However, because of the shortest edge length of the exposed electrodes for this test case, the coverage of the plasma glow over the airfoil surface was found to be the smallest among the four compared test cases. As shown quantitatively in Fig. 11(d), the resultant surface temperature increases (i.e., ΔT values) induced by the DBD plasma actuation were found to be only marginally better than those of the test case #3 (i.e., the test case with the weakest plasma discharge strength but largest plasma glow coverage). Therefore, the layout of test case #5 is not very effective for anti-icing applications either, i.e., with the rivulet-shaped ice structures starting to form at the downstream location of $X/C \approx 66\%$.

By comparing the IR thermal imaging results given in Fig. 11, it can also be seen that, the DBD plasma actuator layout of test case #2, which has both relatively large coverage of the plasma glow and reasonably strong plasma discharge strength, was found to have the highest surface temperature increases over the airfoil surface. As a result, the runback water was found to be able to stay in liquid phase with the longest duration in comparison to all the other test cases, causing the latest formation of the rivulet-shaped ice structures on the rear surface of the airfoil/wing model (i.e., starting at the furthest downstream location of $X/C \approx 78\%$). In summary, for the same protected area over the airfoil surface and same power inputs supplied to the DBD plasma actuators, the

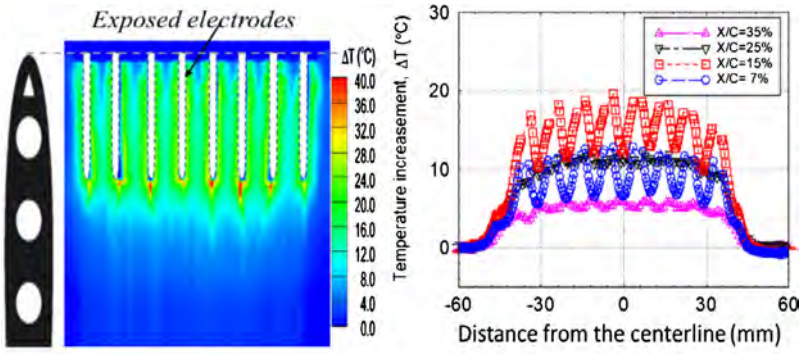

(a). Test case #3 with N= 8, W=2 mm

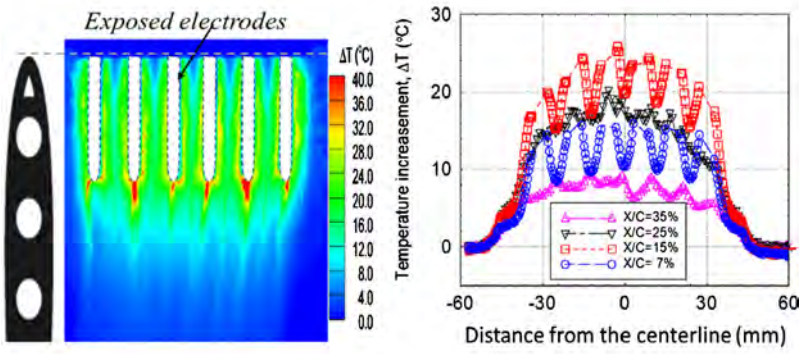

(b.). Test case #2 with N=6, W=4 mm

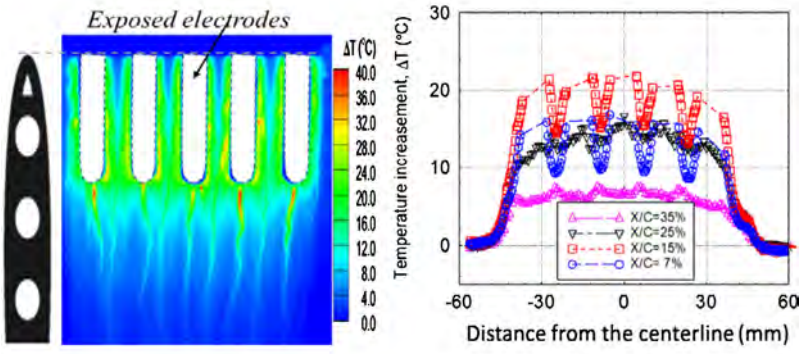

(c). Test case #4 with N= 5, W=6 mm

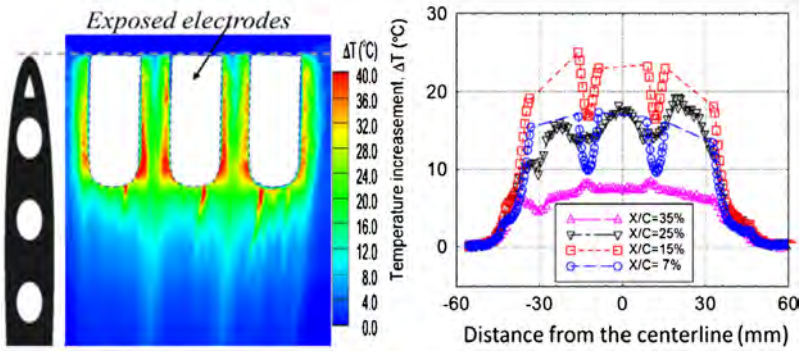

(d). Test case #5 with N=3, W=16 mm

Fig. 11. Acquired IR thermal imaging results and the extracted temperature profiles for the compared test cases under the test condition of with $V_\infty = 40$ m/s, $T_\infty = -5.0\,^\circ$C and LWC=1.5 g/m^3.

layout of the test case #2 was found to have the best anti-icing performance among the four compared test cases.

4. Conclusions

An experimental study was conducted to characterize the effects of the layout of DBD plasma actuators embedded over the front surface of an airfoils/wing model on the plasma-induced thermal characteristics and evaluate their anti-icing performance for aircraft icing mitigation. The experiments were conducted by leveraging an Icing Research Tunnel of Iowa State University to generate a typical glaze icing condition pertinent to aircraft icing phenomena. An array of plasma actuators wrapped around the leading edge of an airfoil/wing model was used for the experimental campaign. The plasma actuators were arranged in different layouts (i.e., different orientation, total number, and width of the exposed electrodes) to assess their effects on the anti-icing performance under the glaze icing condition. While the dynamics ice accretion or anti-icing process over the airfoil surface before and after turning on the plasma actuators was recorded by using a high-resolution imaging system, a high-speed IR thermal imaging system was also used to map the corresponding temperature distributions over the airfoil surface.

The experimental results reveal clearly that, with the same power inputs supplied for the anti-icing operation, the plasma actuators in streamwise layout would induce higher surface temperatures on the airfoil surface and have a noticeably better anti-icing performance than those in spanwise layout. This can be explained by the facts that plasma actuator layout would greatly affect the characteristics of the plasma-induced wall jets interacting with the incoming airflow, thereby, inflecting the dissipation of the plasma-induced gas heating over the airfoil surface substantially. With the plasma actuators in spanwise layout, the dynamic interactions between the plasma-induced wall jets and the incoming airflow would cause the formation of spanwise vortex structures along the spanwise-oriented edges of the exposed electrodes, resulting in greater disturbances to the incoming airflow over the airfoil surface. This would promote a faster transition of the boundary layer airflow over the airfoil surface to turbulence, or/and increase the turbulence intensity levels in the airflow. Associated with the more turbulent airflow over the airfoil surface, the plasma-induced gas heating would be dissipated much faster via the enhanced convective heat transfer from the heated airfoil surface to the frozen-cold airflow. Therefore, with the same power inputs supplied to the plasma actuators, due to the enhanced convective heat transfer, the airfoil surface temperatures for the test case with the plasma actuators in spanwise layout were found to be noticeably lower than those of the streamwise layout case. Furthermore, the spanwise-oriented exposed electrodes would also block or slow down the runback of the surface water, increasing the possibility of the runback surface water to be frozen into rivulet-shaped ice structures before being shed off from the airfoil trailing edge. In comparison, the streamwise layout streamwise-oriented plasma actuators (i.e., in streamwise layout) would enable a much smoother flowing of the air streams and runback water over the airfoil surface. As a result, the plasma actuators in streamwise layout were found not only to be able to prevent ice formation/accretion near the airfoil leading edge, but also allow the plasma-induced thermal effects to convect further downstream to effectively delay/prevent the formation/accretion of runback ice on the rear surface of the airfoil/wing model.

It was also found that, with a fixed power input supplied for DBD plasma actuation, while the layout with greater number of plasma actuators would increase the coverage of plasma glow (i.e., larger coverage of the plasma-induced gas heating on the airfoil surface), the strength of the plasma discharge was found to become weaker (i.e., less plasma-induced surface temperature increases), resulting in a poor anti-icing performance. On the other hand, while the layout with less number of the plasma actuators would increase the strength of the plasma discharges, the smaller coverage of the plasma glow over the airfoil surface would also compromise its effectiveness for anti-icing operation. An optimized layout with a proper balance between the strength of the generated plasma discharges and the coverage of the plasma glow would result in the best anti-icing performance.

It should be noted that, while many interesting findings about the effects of the DBD plasma actuator layout on the plasma-induced thermal characteristics and the resultant anti-icing performance have been derived via the present study, much more fundamental researches are still needed to gain further insights into the complex interactions between DBD plasma discharges with frozen-cold air, liquid water and solid ice in the context of aircraft anti-/de-icing. For example, the present experimental campaign was conducted at the chord Reynolds number of $Re_c \approx 500{,}000$. While the Reynolds number level is within the range of lightweight, unmanned-aerial-vehicles (UAVs), it is much lower than those of large-sized, manned aircraft. While the general trend about the layout effects of the plasma actuators on their anti-icing effectiveness is expected to be the same for the scenario with higher Reynolds numbers, a systematic study will be conducted in the near future to characterize the effects of the Reynold numbers on the effectiveness of the DBD plasma actuators for aircraft icing mitigation.

It should also be noted that, in addition to the plasma-induced thermal effects, DBD actuators can also induce ionic secondary flows over airfoil surface and have been widely used as active flow control devices to suppress flow separation and/or delay airfoil stall for improved aerodynamic performance. Therefore, with the same sets of DBD plasma actuators embedded over airfoil/wing surfaces, they could be used for dual purposes. The plasma actuators can be used as active flow control devices to suppress boundary layer flow separation and/or delay airfoil stall for improved aerodynamic performance under conventional, non-icing conditions. Meanwhile, they can also be functionalized as effective anti-icing devices to prevent ice formation over the airfoil surface under icing conditions to ensure safer and more efficient operation of both manned and unmanned aircraft in cold weathers.

CRediT authorship contribution statement

Cem Kolbakir: Icing tunnel experiments, Model design and manufacture, Data acquisition and processing, Formal analysis, Writing - original draft. Haiyang Hu: Icing tunnel experiments, Data acquisition and processing. Yang Liu: Data processing & analysis, Formal analysis. Hui Hu: Conceptualization, Methodology, Formal analysis, Writing – review & editing, Funding acquisition, Supervision.

Declaration of competing interest

The authors declare that they have no competing interest.

Acknowledgements

The research work is partially supported by Iowa Energy Center for Wind Turbine Icing Study under the IEC Competitive Grant # 312350 and National Science Foundation (NSF) under award numbers of CBET-1935363 and CBET-1916380.

References

[1] Y. Cao, W. Tan, Z. Wu, Aircraft icing: an ongoing threat to aviation safety, Aerosp. Sci. Technol. 75 (2018) 353–385, https://doi.org/10.1016/j.ast.2017.12.028.

[2] M.B. Bragg, G.M. Gregorek, J.D. Lee, Airfoil aerodynamics in icing conditions, J. Aircr. 23 (1986), https://doi.org/10.2514/3.45269.

[3] D.I. Ignatyev, A.N. Khrabrov, A.I. Kortukova, D.A. Alieva, M.E. Sidoryuk, S.G. Bazhenov, Interplay of unsteady aerodynamics and flight dynamics of transport aircraft in icing conditions, Aerosp. Sci. Technol. 104 (2020) 105914, https://doi.org/10.1016/j.ast.2020.105914.

[4] A. Lampton, J. Valasek, Prediction of icing effects on the lateral/directional stability and control of light airplanes, Aerosp. Sci. Technol. 23 (2012) 305–311, https://doi.org/10.1016/j.ast.2011.08.005.

[5] D.L. Kohlman, W.G. Schweikhard, P. Evanich, Icing-tunnel tests of a glycol-exuding, porous leading-edge ice protection system, J. Aircr. 19 (1982) 647–654, https://doi.org/10.2514/3.57445.

[6] S.K. Thomas, R.P. Cassoni, C.D. MacArthur, Aircraft anti-icing and de-icing techniques and modeling, J. Aircr. 33 (1996) 841–854, https://doi.org/10.2514/3.47027.

[7] L.M. Nicolai, C.A. Martin, J.C. Puttt, Advanced pneumatic impulse ice protection system (PUP) for aircraft, J. Aircr. 29 (1991) 714–716, https://doi.org/10.2514/3.46227.

[8] J.M. Brown, S. Raghunathan, J.K. Watterson, A.J. Linton, D. Riordon, Heat transfer correlation for anti-icing systems, J. Aircr. 39 (2002), https://doi.org/10.2514/2.2896.

[9] F. Zhang, W. Deng, H. Nan, L. Zhang, Z. Huang, Reliability analysis of bleed air anti-icing system based on subset simulation method, Appl. Therm. Eng. 115 (2017) 17–21, https://doi.org/10.1016/j.applthermaleng.2016.11.202.

[10] L. Makkonen, Surface melting of ice, J. Phys. Chem. B 101 (1997) 6196–6200, https://doi.org/10.1021/JP963248C.

[11] L. Chen, Y. Zhang, Q. Wu, Heat transfer optimization and experimental validation of anti-icing component for helicopter rotor, Appl. Therm. Eng. 127 (2017) 662–670, https://doi.org/10.1016/j.applthermaleng.2017.07.169.

[12] J. Wang, Z. Lu, Y. Shi, Aircraft icing safety analysis method in presence of fuzzy inputs and fuzzy state, Aerosp. Sci. Technol. 82–83 (2018) 172–184, https://doi.org/10.1016/j.ast.2018.09.003.

[13] L. Ma, Z. Zhang, L. Gao, Y. Liu, H. Hu, Bio-inspired icephobic coatings for aircraft icing mitigation: a critical review, Rev. Adhes. Adhes. 8 (2020) 168–199, https://doi.org/10.7569/RAA.2020.097307.

[14] Y.H. Yeong, A. Milionis, E. Loth, J. Sokhey, Self-lubricating icephobic elastomer coating (SLIC) for ultralow ice adhesion with enhanced durability, Cold Reg. Sci. Technol. 148 (2018) 29–37, https://doi.org/10.1016/j.coldregions.2018.01.005.

[15] Y. Liu, L. Li, H. Li, H. Hu, An experimental study of surface wettability effects on dynamic ice accretion process over an UAS propeller model, Aerosp. Sci. Technol. 73 (2018) 164–172, https://doi.org/10.1016/j.ast.2017.12.003.

[16] H. Sojoudi, M. Wang, N.D. Boscher, G.H. McKinley, K.K. Gleason, Z.Z. Yang, G.H. McKinley, K.K. Gleason, F. Liu, M.L. Hu, S.R. Hunter, J.A. Haynes, K.K. Gleason, Durable and scalable icephobic surfaces: similarities and distinctions from superhydrophobic surfaces, Soft Matter 12 (2016) 1938–1963, https://doi.org/10.1039/C5SM02295A.

[17] D.L. Beemer, W. Wang, A.K. Kota, M. Doi, F. Brochard-Wyart, A. Tuteja, J. Aizenberg, J. Wang, Y. Song, L. Jiang, Durable gels with ultra-low adhesion to ice, J. Mater. Chem. A 4 (2016) 18253–18258, https://doi.org/10.1039/C6TA07262C.

[18] T.C. Corke, C.L. Enloe, S.P. Wilkinson, Dielectric barrier discharge plasma actuators for flow control*, Annu. Rev. Fluid Mech. 42 (2010) 505–529, https://doi.org/10.1146/annurev-fluid-121108-145550.

[19] A. Ebrahimi, M. Hajipour, Flow separation control over an airfoil using dual excitation of DBD plasma actuators, Aerosp. Sci. Technol. 79 (2018) 658–668, https://doi.org/10.1016/j.ast.2018.06.019.

[20] J.-J. Wang, K.-S. Choi, L.-H. Feng, T.N. Jukes, R.D. Whalley, Recent developments in DBD plasma flow control, Prog. Aerosp. Sci. 62 (2013) 52–78, https://doi.org/10.1016/j.paerosci.2013.05.003.

[21] M.G. De Giorgi, V. Motta, A. Suma, Influence of actuation parameters of multi-DBD plasma actuators on the static and dynamic behaviour of an airfoil in unsteady flow, Aerosp. Sci. Technol. 96 (2020) 105587, https://doi.org/10.1016/j.ast.2019.105587.

[22] N. Benard, E. Moreau, Electrical and mechanical characteristics of surface AC dielectric barrier discharge plasma actuators applied to airflow control, Exp. Fluids 55 (2014) 1846, https://doi.org/10.1007/s00348-014-1846-x.

[23] F. Rodrigues, J. Pascoa, M. Trancossi, Heat generation mechanisms of DBD plasma actuators, Exp. Therm. Fluid Sci. 90 (2018) 55–65, https://doi.org/10.1016/J.EXPTHERMFLUSCI.2017.09.005.

[24] W. Zhou, Y. Liu, H. Hu, H. Hu, X. Meng, Utilization of thermal effect induced by plasma generation for aircraft icing mitigation, AIAA J. 56 (2018) 1–8, https://doi.org/10.2514/1.J056358.

[25] Y. Liu, C. Kolbakir, H. Hu, A. Starikovskiy, R.B. Miles, An experimental study on the thermal characteristics of NS-DBD plasma actuation and application for aircraft icing mitigation, Plasma Sources Sci. Technol. (2018), https://doi.org/10.1088/1361-6595/aaedf8.

[26] Y. Liu, C. Kolbakir, H. Hu, H. Hu, A comparison study on the thermal effects in DBD plasma actuation and electrical heating for aircraft icing mitigation, Int. J. Heat Mass Transf. 124 (2018) 319–330, https://doi.org/10.1016/J.IJHEATMASSTRANSFER.2018.03.076.

[27] X. Meng, H. Hu, C. Li, A.A. Abbasi, J. Cai, H. Hu, Mechanism study of coupled aerodynamic and thermal effects using plasma actuation for anti-icing, Phys. Fluids 31 (2019) 037103, https://doi.org/10.1063/1.5086884.

[28] J. Cai, Y. Tian, X. Meng, X. Han, D. Zhang, H. Hu, An experimental study of icing control using DBD plasma actuator, Exp. Fluids 58 (2017) 102, https://doi.org/10.1007/s00348-017-2378-y.

[29] B. Wei, Y. Wu, H. Liang, Y. Zhu, J. Chen, G. Zhao, H. Song, M. Jia, H. Xu, SDBD based plasma anti-icing: a stream-wise plasma heat knife configuration and criteria energy analysis, Int. J. Heat Mass Transf. 138 (2019) 163–172, https://doi.org/10.1016/j.ijheatmasstransfer.2019.04.051.

[30] J. Little, K. Takashima, M. Nishihara, I. Adamovich, M. Samimy, Separation control with nanosecond-pulse-driven dielectric barrier discharge plasma actuators, AIAA J. 50 (2012) 350–365, https://doi.org/10.2514/1.J051114.

[31] K. Kourtzanidis, L.L. Raja, Three-electrode sliding nanosecond dielectric barrier discharge actuator: modeling and physics, AIAA J. 55 (2017) 1393–1404, https://doi.org/10.2514/1.J055473.

[32] X. Meng, L. Hou, L. Wang, M. MacAlpine, G. Fu, B. Sun, Z. Guan, W. Hu, Y. Chen, Oscillation of conductors following ice-shedding on UHV transmission lines, Mech. Syst. Signal Process. 30 (2012) 393–406, https://doi.org/10.1016/J.YMSSP.2011.10.020.

[33] J. Chen, H. Liang, Y. Wu, B. Wei, G. Zhao, M. Tian, L. Xie, Experimental study on anti-icing performance of NS-DBD plasma actuator, Appl. Sci. 8 (2018), https://doi.org/10.3390/app8101889.

[34] Y. Tian, Z. Zhang, J. Cai, L. Yang, L. Kang, Experimental study of an anti-icing method over an airfoil based on pulsed dielectric barrier discharge plasma, Chin. J. Aeronaut. (2018), https://doi.org/10.1016/j.cja.2018.05.008.

[35] R.M. Waldman, H. Hu, High-speed imaging to quantify transient ice accretion process over an airfoil, J. Aircr. 53 (2016) 369–377, https://doi.org/10.2514/1.C033367.

[36] L. Gao, Y. Liu, H. Hu, An experimental investigation on the dynamic glaze ice accretion process over a wind turbine airfoil surface, Int. J. Heat Mass Transf. 149 (2020) 119120, https://doi.org/10.1016/J.IJHEATMASSTRANSFER.2019.119120.

[37] L. Li, Y. Liu, L. Tian, H. Hu, H. Hu, X. Liu, I. Hogate, A. Kohli, An experimental study on a hot-air-based anti-/de-icing system for aero-engine inlet guide vanes, Appl. Therm. Eng. 167 (2020) 114778, https://doi.org/10.1016/j.applthermaleng.2019.114778.

[38] R. Veerakumar, L. Gao, Y. Liu, H. Hu, Dynamic ice accretion process and its effects on the aerodynamic drag characteristics of a power transmission cable model, Cold Reg. Sci. Technol. 169 (2020) 102908, https://doi.org/10.1016/j.coldregions.2019.102908.

[39] Y. Liu, H. Hu, An experimental investigation on the unsteady heat transfer process over an ice accreting airfoil surface, Int. J. Heat Mass Transf. 122 (2018) 707–718, https://doi.org/10.1016/j.ijheatmasstransfer.2018.02.023.

[40] R. Joussot, D. Hong, H. Rabat, V. Boucinha, R. Weber-Rozenbaum, A. Leroy-Chesneau, Thermal characterization of a DBD plasma actuator: dielectric temperature measurements using infrared thermography, in: 40th AIAA Fluid Dyn. Conf., 2010.

[41] Y. Liu, L. Li, W. Chen, W. Tian, H. Hu, An experimental study on the aerodynamic performance degradation of a UAS propeller model induced by ice accretion process, Exp. Therm. Fluid Sci. 102 (2019) 101–112, https://doi.org/10.1016/j.expthermflusci.2018.11.008.

[42] L. Gao, Y. Liu, L. Ma, H. Hu, A hybrid strategy combining minimized leading-edge electric-heating and superhydro-/ice-phobic surface coating for wind turbine icing mitigation, Renew. Energy 140 (2019) 943–956, https://doi.org/10.1016/J.RENENE.2019.03.112.

[43] T.C. Corke, C.L. Enloe, S.P. Wilkinson, Dielectric barrier discharge plasma actuators for flow control, Annu. Rev. Fluid Mech. 42 (2010) 505–529, https://doi.org/10.1146/annurev-fluid-121108-145550.

[44] T.N. Jukes, K.-S. Choi, On the formation of streamwise vortices by plasma vortex generators, J. Fluid Mech. 733 (2013) 370–393, https://doi.org/10.1017/jfm.2013.418.

[45] K. Zhang, T. Wei, H. Hu, An experimental investigation on the surface water transport process over an airfoil by using a digital image projection technique, Exp. Fluids 56 (2015) 173, https://doi.org/10.1007/s00348-015-2046-z.

[46] T.C. Corke, C.L. Enloe, S.P. Wilkinson, Dielectric barrier discharge plasma actuators for flow control, Annu. Rev. Fluid Mech. 42 (2010) 505–529, https://doi.org/10.1146/annurev-fluid-121108-145550.

[47] R. Dawson, J. Little, Characterization of nanosecond pulse driven dielectric barrier discharge plasma actuators for aerodynamic flow control, J. Appl. Phys. 113 (2013), https://doi.org/10.1063/1.4794507.

[48] F.F. Rodrigues, J.C. Pascoa, M. Trancossi, Experimental analysis of dielectric barrier discharge plasma actuators thermal characteristics under external flow influence, J. Heat Transf. 140 (2018), https://doi.org/10.1115/1.4040152.